Science of the Total Environment 956 (2024) 177225

Contents lists available at ScienceDirect

Science of the Total Environment

journal homepage: www.elsevier.com/locate/scitotenv

Automated estimation of offshore polymetallic nodule abundance based on seafloor imagery using deep learning

Arkadiusz Tomczak [a,*], Tomasz Kogut [a], Karol Kabała [a], Tomasz Abramowski [a], Jakub Ciążela [b], Andrzej Giza [c]

[a] Maritime University of Szczecin, Wały Chrobrego 1-2, 70-500 Szczecin, Poland
[b] Institute of Geological Sciences, Polish Academy of Sciences, ul. Podwale 75, 50-449 Wrocław, Poland
[c] Institute of Marine and Environmental Sciences, University of Szczecin, Mickiewicza 16, 70-383 Szczecin, Poland

HIGHLIGHTS

- Provides a time-efficient and automatized deep learning method for seafloor polymetallic nodules abundance estimation as an alternative to expert visual evaluation of large data set of seafloor photographs.
- Provides a web-based tool to annotate polymetallic nodules on seafloor photographs to collect the learning data (labels) that combines expert knowledge and process automatization.

GRAPHICAL ABSTRACT

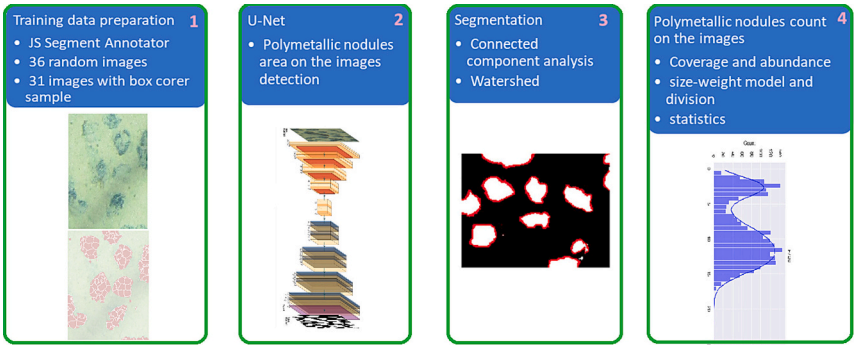

ARTICLE INFO

Editor: Julian Blasco

Keywords:
Seafloor polymetallic nodules
Abundance estimation
Deep learning image analysis

ABSTRACT

The burgeoning demand for critical metals used in high-tech and green technology industries has turned attention toward the vast resources of polymetallic nodules on the ocean floor. Traditional methods for estimating the abundance of these nodules, such as direct sampling or acoustic imagery are time and labour-intensive or often insufficient for large-scale or accurate assessment. This paper advocates for the automatization of polymetallic nodules detection and abundance estimation using deep learning algorithms applied to seabed photographs.

We propose UNET convolutional neural network framework specifically trained to process the unique features of seabed imagery, which can reliably detect and estimate the abundance of polymetallic nodules based on thousands of seabed photographs in significantly reduced time (below 10 h for 30 thousand photographs). Our approach addresses the challenges of data preparation, variable image quality, coverage-abundance transition model and sediments presence.

We indicated the utilization of this approach can substantially increase the efficiency and accuracy of resource estimation, dramatically reducing the time and cost currently required for manual assessment. Furthermore, we

* Corresponding author.
E-mail addresses: a.tomczak@pm.szczecin.pl (A. Tomczak), t.kogut@pm.szczecin.pl (T. Kogut), k.kabala@pm.szczecin.pl (K. Kabała), t.abramowski@pm.szczecin.pl (T. Abramowski), j.ciazela@twarda.pan.pl (J. Ciążela), andrzej.giza@usz.edu.pl (A. Giza).

https://doi.org/10.1016/j.scitotenv.2024.177225
Received 27 February 2024; Received in revised form 12 September 2024; Accepted 24 October 2024

discuss the potential of this method to be integrated into large-scale systems for sustainable exploitation of these undersea resources.

1. Introduction

The European Commission has introduced regulations to align EU policies with efforts to combat environmental degradation and climate change. This involves measures to reduce greenhouse gas emissions. The transition to the economy reliant on renewable sources requires significant amounts of elements like copper, nickel, cobalt, zinc, lithium, and rare earth elements. However, terrestrial resources are heavily exploited or unsustainably managed. As a result, deep sea minerals including polymetallic nodules, cobalt-rich crusts, and massive sulphides on the seafloor, have been studied for years as alternative sources (Hein et al., 2013; Mucha et al., 2011; Milinovic et al., 2021).

Deep-sea polymetallic nodules are seen as a promising source of metals needed to support global population growth, urbanization, high-tech applications, and a sustainable green economy (Hein et al., 2013; Sakellariadou et al., 2022; Volkmann et al., 2018).

However, deep ocean mining can be complex in many aspects. To assess the viability of such operations, it's crucial to understand the quantity and quality of these underwater resources, to develop effective extraction methods and mitigation strategies to minimize environmental impact, as well as to evaluate the economic potential, metallurgical processing, and metals markets (Parianos et al., 2021).

Although no commercial-scale deep- sea mining has occurred, many mining operations are active in the shallow waters (Miller et al., 2018). Exact resource assessment can be challenging in the deep ocean due to the harsh environment and the difficulties in accessing the seabed (Weaver et al., 2022). However, several methods exist to assess nodule resources, including: seafloor photography, acoustic data, local gravimetry data and direct sampling (Alevizos et al., 2018; Gazis et al., 2018; Peukert et al., 2018; Kuhn et al., 2020). Direct methods involve physically sampling the seabed to collect and count nodules. This can be done using a variety of tools, such as box corers orgrab samplers (Mucha and Wasilewska-Błaszczyk, 2020). Direct methods are assumed the most accurate way to assess nodule abundance but are also the most time-consuming and expensive.

1.1. Exploration methods

Remote (indirect) sensing involves seafloor photography and acoustic data. The methods can be used to map the seabed nodule distribution to estimate their size and density. Multibeam echosounder or sonar backscatter intensities correlate well with the abundance of polymetallic nodules. Some of the seabed features like high slope gradient and basement outcrops may result in worse recognition (Yoo et al., 2018). Indirect methods are proven less accurate than direct methods, but they are much faster and cheaper (Gazis et al., 2018; Mucha and Wasilewska-Błaszczyk, 2020; Parianos et al., 2021; Tsune, 2021; Wong et al., 2021; Yoo et al., 2018). Combining these technologies allows mining companies to better assess nodule resources, enabling informed decisions on mining feasibility and the development of measures to minimize environmental impact.

The most studied polymetallic nodule area is Clarion and Clipperton Fracture Zones (CCZ), where enormous quantities of these nodules were observed, conservatively estimated to total 21 billion dry tons (Hein et al., 2020).

Within this region, the international consortium Interoceanmetal Joint Organization (IOM), has the right to conduct exploration activities on two sectors located in the Pacific, with a total area of 75,000 km^2, (Mucha et al., 2011). IOM's information include datasets based on which, preliminary resource estimates can be made. Published estimates are based on data from seafloor samples taken with a box corer (Gazis et al., 2018; Mucha et al., 2011). The high costs and labour intensity of direct sampling limit the number of collected samples and the accuracy of estimates, particularly in smaller areas. Since bottom sampling provides only point measurements, it doesn't offer comprehensive information on resource assessment. Therefore, it's rational to complement it with hydro-acoustic methods, bathymetry, backscatter, side-scan sonar, and bottom photography (Rühlemann et al., 2011; Wong et al., 2017; Mucha and Wasilewska-Błaszczyk, 2020; Sharma et al., 2010; Wasilewska-Błaszczyk and Mucha, 2020).

In the IOM area, attempts have already been made to estimate resources based on Red-Green-Blue images (RGB) concurrently assessing the feasibility of using this type of data for estimation, similar to what was done in other areas of research (Tsune and Okazaki, 2014; Wasilewska-Błaszczyk and Mucha, 2020). Using images for estimation is the next step to further improve the assessment. Most contractors operating within the CCZ collected many photographs over the years, and some have been used for estimation to some extent. Photographically collected data is considered “soft” supplementary data, but there is no clear methodology on how these data can be used for quantitative assessment.

Given the cost-effectiveness of surveys, a large number of photographs can be as helpful, or even more so, than a few expensive samples. In this paper, the authors explore this idea by investigating whether deep learning can estimate coverage and abundance from bottom photographs (Ellefmo and Kuhn, 2021; Felix, 1980; Wasilewska-Błaszczyk and Mucha, 2021).

1.2. Image processing

Photo processing methods in the literature can be categorized into three groups: non-automated, partially automated, and fully automated. Non-automated methods rely on expert evaluation, making them subjective and variable, depending on the evaluator's experience and condition (Sharma et al., 2013). The parameters determined from photos are used in regression models to describe the relationship between visible coverage and real samples, considering nodule coverage, expert assessments, and the genetic type and size of the nodules (Wasilewska-Błaszczyk and Mucha, 2020, 2021).

These methods are low in accuracy and unsuitable for large-scale image analysis, as they rely on expert evaluation and cannot be automated.

In detecting other minerals, alternatives to non-automatic are semi-automatic and automatic methods where segmentation is a critical step in Digital Rock Physics (DRP) (Karimpouli and Tahmasebi, 2019).

1.3. Coverage assessment

Image coverage evaluation relies on computer vision (CV) algorithms for nodule detection and segmentation. However, automating this process can introduce systematic errors in estimating nodule sizes and quantities, influenced by the chosen image processing strategies. Threshold values for distinguishing nodules from sediments based on color contrast also vary with different strategies (Tsune and Okazaki, 2014). Scattering and color change are two major problems of distortion for underwater imaging (Serikawa and Lu, 2014). To address issue of uneven illumination and morphological defects caused by white sand coverage in nodule images, a “background grey value calculation” (Hade et al., 2020) was proposed. Despite advancements like photo augmentation and a new underwater model to correct attenuation, using CV methods remains complex. A fast joint trigonometric filtering dehazing algorithm was also introduced, resulting in enhanced images with

reduced noise, better dark region exposure, improved global contrast, and sharper details (Serikawa and Lu, 2014).

Other researchers observed the traditional segmentation algorithms have insufficient performance in the face of adhesion, and the segmentation boundary is fuzzy (Song et al., 2019). The novel two-stage diffusion-based model for nodule image segmentation, and a linear regression model for predicting nodule abundance based on the coverage obtained through nodule segmentation indicated promising results (Shao et al., 2023). It is worth noting that the development of automated detection algorithms enabled quantitative optical image data analysis and subsequent statistical interpretation of nodule densities. The spatial coverage of optical imaging is much higher than box core sampling (Gazis et al., 2018). However, a comparison of the automated analysis of the images with the data from box core samples showed that nodule abundances derived from the images can underestimate the true values by a factor of up to 5 (Kuhn and Rühlemann, 2021).

The use of neural networks methods to assess polymetallic nodule abundance based on seabed photographs is a relatively new area of research. The recent results of segmentation performed using machine learning (ML) methods, including unsupervised neural network segmentation or unsupervised deep learning, have been presented below.

The core algorithm for such seafloor image analysis with a particular focus on nodules coverage estimation is the so-called hyperbolic self-organising map (HSOM) neural network approach (Kuhn and Rühlemann, 2021). Other approach addressed challenge by combining high resolution hydroacoustic and optical data sets acquired with an autonomous underwater vehicle (AUV) and connecting those data with a machine learning (ML) algorithm (here random forests), in order to predict the spatial distribution of the number of nodules per square meter (Gazis et al., 2018). Evolutionary tuned Segmentation (ES4C) using Cluster Co-occurrence and a Convexity Criterion method for a fully automated segmentation of benthic images to polymetallic nodules and sediment background is introduced. ES4C is based on an arbitrary feature representation and vector quantization algorithm. Through prototype assignments a binary image segmentation function is constructed in a data-driven way without manual prototype annotation. Possible assignments are explored with the genetic algorithm to provide a heuristic solution based on an efficiently computable fitness measure (Schoening et al., 2016). Due to their automatic process, they are suitable for analyzing large amounts of data and have a higher accuracy of coverage assessment. CV or unsupervised ML algorithms perform worse than the expert when there is partial coverage of nodules by sediment, and their accuracy is correlated with the quality of the images, including their variable illumination and variable angle of capture. This translates into the possibility of reduced under coverage detection.

Therefore, combination expert knowledge with supervised deep learning seemed to the authors an approach that should overcome the disadvantages of manual and unsupervised methods while maintaining full automation of the process and accuracy.

This paper presents our newly developed automatic method for estimating polymetallic nodule resources from seafloor's RGB images (photographs) using supervised deep-learning methods (Liu et al., 2021).

The automation of the learning data collection process using a web application of the slic superpixel algorithm enabled accurate determination of nodules and efficient collection of an extensive learning set of about 1440 photos in the form of two binary classes 0 - no nodules and 1-nodules analogous to those of Song et al. (Song et al., 2019). The analysis of learning curves resulted in the selection of CNN network hyperparameters and the development of a deep model, in which 31,000 seafloor images were processed. Coverage of the images with nodules was determined, and then based on the watershed and connected component analysis (CCA) algorithm, fields of connected nodules were segmented into single instances. The mass of the nodules was determined based on a transition model from percent area coverage to abundance expressed in kg/m^2. The photos processed in this way made it possible to determine the nodules' coverage, mass, granulation and many other parameters necessary for the overall resource assessment.

2. Materials

Our study was performed for the exploration area (75,000 km^2) of the Interoceanmetal Joint Organization consortium (IOM), one of the 19 International Seabed Authority (ISA) contractors for nodules situated in the Clarion-Clipperton Zone exploration area (~4,500,000 km^2) (Rühlemann et al., 2011) (Fig. 1).

The CCZ is the most critical and explored nodule field worldwide (Parianos et al., 2021). The CCZ constitutes an abyssal plain between 4000 and 5000 m deep. The IOM area is composed of two sectors situated in the eastern part of the CCZ exploration areas between German, Singapore, and Nauru contract areas, a smaller B1 in the north (12,000 km^2) and B2 sector in the north (63,000 km^2), (Wasilewska-Błaszczyk and Mucha, 2020). The spatial distribution of mineralized material is essential for a reliable estimation of mineral resources. Although the area of polymetallic nodules is enormous, nodules are not equally developed or preserved on all parts of the seafloor (Parianos et al., 2021). We focus on the H22 exploration block (~4200 km^2) of the B2 sector with 12 image survey lines and H33 block with 2 image survey lines and area East of H44 with another 2 image survey lines. This block, together with block H11 (5300 km^2), is one of the most prospective mining fields selected for future exploitation due to high nodule abundance significantly exceeding 10 kg/m^2 (Wasilewska-Błaszczyk and Mucha, 2020).

The northeastern corner of the H22 block, as presented constitutes 37 % (~1560 km^2) of the H22 area. It is mostly plateau-like abyssal plain with two groups of seamounts in the east and south, as well as a sparsely distributed parallel ridge and grabens oriented NNW-SSE to N-S.

One-tenth of the study area (~150 km^2) is covered by seamounts and volcanic cones associated with hard-rock basaltic or diabase exposures (Maciąg et al., 2019) and sometimes a chalk layer in between the soft sediments and volcanic basement (Parianos et al., 2021) indicated by our backscatter data. The remaining 90 % (1410 km^2) is a sediment-covered area, typically smooth and flat, and is most interesting from nodule exploration. Most (~1190 km^2) of it is embedded with nodules. The related sediments are typically pelagic clay and siliceous ooze (Wasilewska-Błaszczyk and Mucha, 2020) with trace amounts of coarser-grained detrital and allochthonous volcanic material (Maciąg et al., 2019)Interestingly the sediments are poor in metals, with only ~6 % iron and ~0.5 % manganese, which may be owed to the diagenetic "scavenging" of metals by the nodules. The sedimentation rate in the CCZ area is suggested to be 0.35–0.50 cm/kyr (Ellefmo and Kuhn, 2021).

These areas are affected by seabed currents that drift and accumulate sediments, mostly fine clays and oozes (Parianos et al., 2021). The advantage of polymetallic nodules in the Pacific Ocean is their high content of three primary metals: Ni, Cu, Co, and, Mn, combined with contents of Mo, Ti, Li, V, and REE, which can be considered as a by-product if a relevant processing method is used (Kuhn and Rühlemann, 2021). The nodules grow to a size between 1 and 15 cm in diameter on top or within the first 10 cm of deep-sea sediments (Rühlemann et al., 2011), with a spheroidal or elliptical shape and typical sizes of 3–4 cm for hydrogenetic nodules and 6–12 for diagenetic nodules (Wasilewska-Błaszczyk and Mucha, 2020). Hydrogenetic nodules form directly from the precipitation of Fe oxyhydroxides and Mn oxides from oxygen-rich near-bottom seawater (Ellefmo and Kuhn, 2021; Hein et al., 2020). They are enriched in Co and REE (Volkmann et al., 2018). The relative variability of primary metal grades for the IOM area is very low, with a coefficient of 7–11 % variation within the H22 block. It is primarily a result of the stable mineral and chemical composition of nodules.

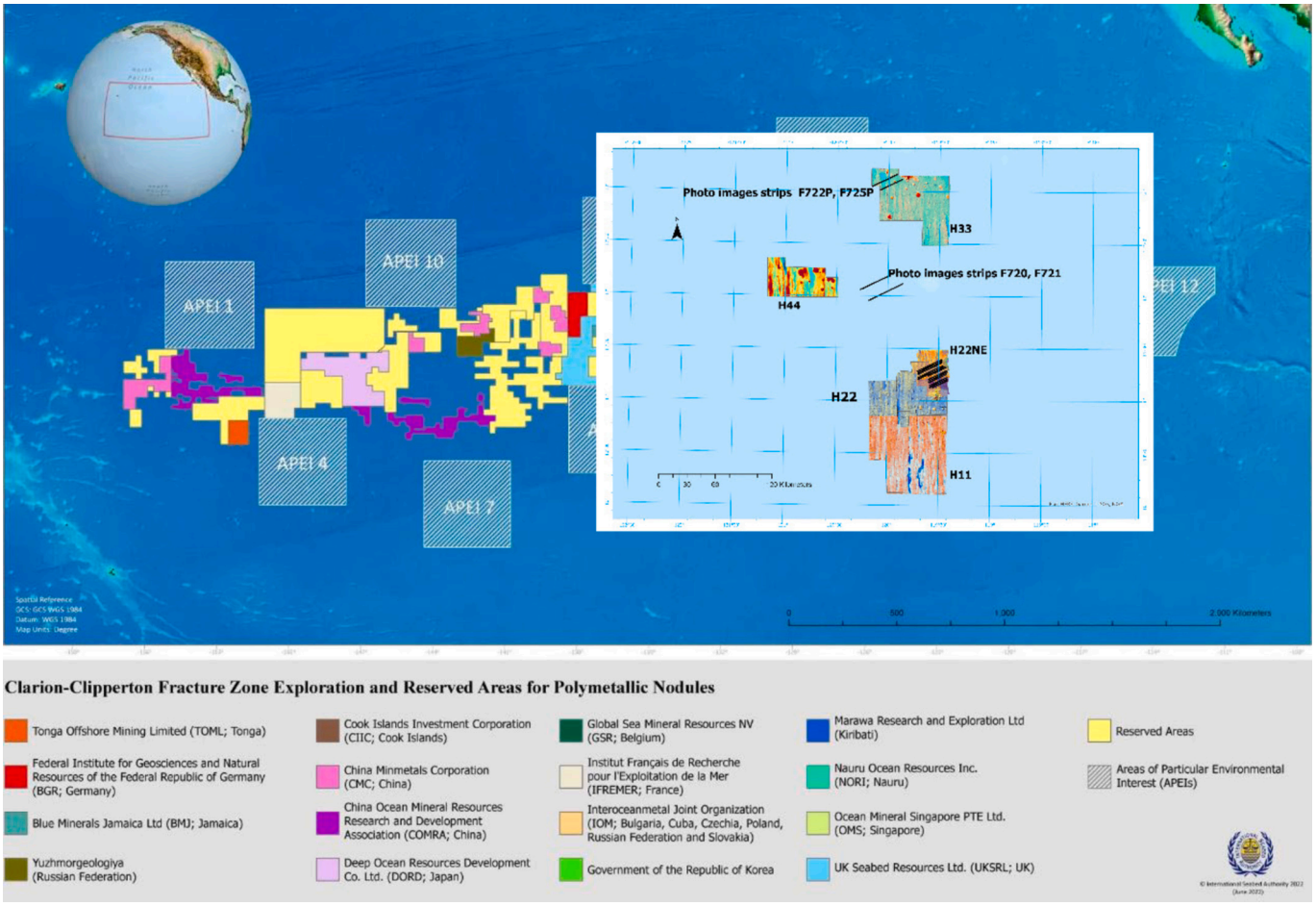

Fig. 1. Location and bathymetry maps of B2 IOM area and exploration blocks: H22, H11, H22NE, H44, H33 (International Seabed Authority, 2018).

3. Methods

3.1. Data acquisition

In 2019, bottom surveys consisting of photographic profiling were conducted on 16 survey lines (rows), and 30,373 bottom images were acquired at a resolution of 5184 × 3456 pixels. 12 survey lines were located in the H22NE area (Fig. 2), 2 lines in the H33 area and another 2 outside the designated areas.

At the same time, 31 bottom samples were taken using a box corer, with simultaneous imaging in a 3648 × 2736 pixel photo. In addition, 17 images with bottom samples at 2592 × 1944 resolution were acquired in

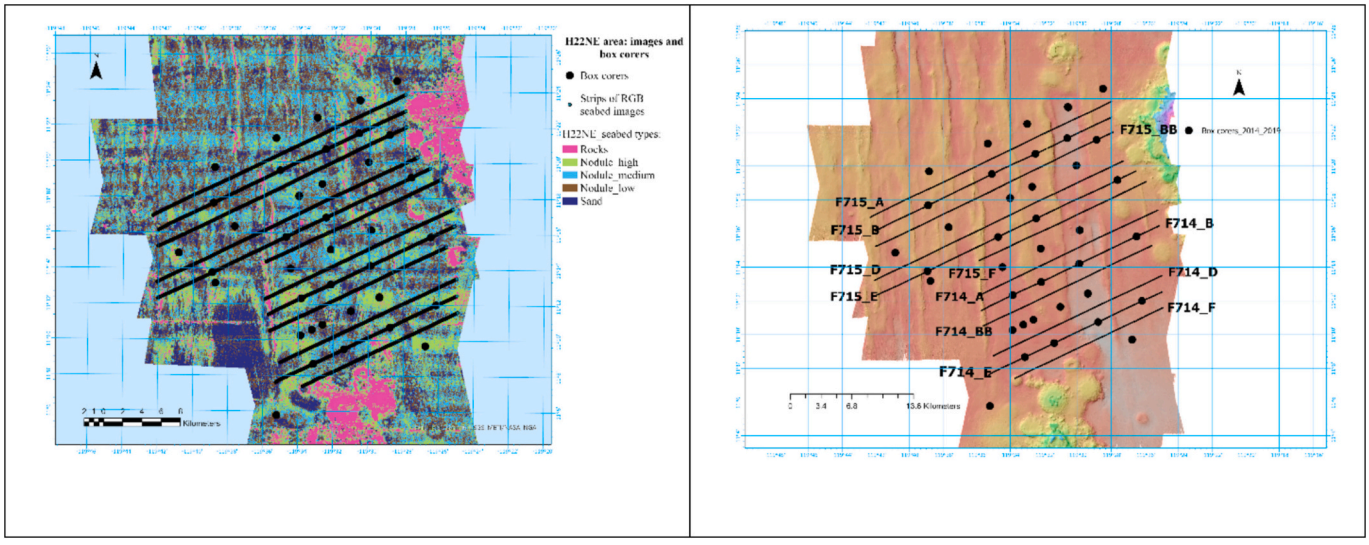

Fig. 2. Classified seabed image (left) and bathymetric image (right) of H22NE exploration block based on backscatter intensity data with photo survey lines and box corers location.

2014 (Fig. 3: (a)). These different data sets provide an important basis for estimating the polymetallic nodules. Bottom samples collected with box corer of 0.5 m × 0.5 m x0.5m dimension (Fig. 3(b)) were used to determine the mass of nodules per square meter, at the collection site. They were manually sorted by experts (Fig. 3: (c)) into classes of 0–20 mm, 20–40 mm, 40–60 mm, 60–80 mm, 80–100 mm, 100–120 mm and their mass was determined. The data acquired this way was used to construct a coverage-abundance model.

3.2. Training data for supervised learning

The training data was prepared using JS Segment Annotator (Fig. 4). This is a tool for manual determination of regions in images, written in the JavaScript programming language and can be used in web browsers. It allows the user to draw a border around the area occupied by a single nodule or a group of them.

Many experts working in the field of image analysis, especially those dealing with nodules, face a challenge in the form of various artefacts, such as sediments, and elements of flora or fauna, which can introduce noise and hinder the work of automatic image processing algorithms (Fig. 5: (a)). To improve the interpretation of such cases and facilitate the work of neural networks, slic superpixels were used in the Java Script Segment Annotator, with the help of which, an expert decided whether and how to label a nodule partially covered with sediment or covered with biological organisms. Typically, based on the experience, the expert labelled the blanketed parts as nodules (Fig. 5: (b) and (c)).

This labelling was intended to provide the neural network, in this case, U-Net, with specific information about the location of the nodules. The labelling of nodules as nodules, even if they are partially covered with the deposit, is crucial for the correct interpretation and classification of objects in an image. U-Net, being a machine learning model, can use this information to recognize and segregate nodules and distinguish them from other elements in the image.

Training data was prepared by expert labelling of nodules visible on images using Java Script Segment Annotator software. The diagram below shows the process of nodule detection model (Fig. 6). It uses a neural network with an architecture similar to the popular UNet.

3.3. UNet model architecture and tuning of hyperparameters

This model was developed for medical engineering and automatic tissue segmentation tasks (Pan et al., 2020; Ronneberger et al., n.d.). It has since become useful and is proving itself in other industries like automotive autonomy or aerial remote sensing. Since its presentation, it has also been successfully used in other industries for example: autonomous cars and aerial remote sensing (Darapaneni et al., 2021; Munawar et al., 2023). For this reason, it is now widely used as the first choice for a segmentation task in any industry, although recently there have been competing solutions, e.g., networks from the YOLO (Carraro et al., 2023; He et al., 2022), SAM or R-CNN family, which in many tasks, after using a technique called transfer learning, give better results (Carraro et al., 2023; Dong et al., 2021; He et al., 2022). However, it was decided to use it, as a proven method, in the first iteration of the work. The

Fig. 3. Photo of nodules on bottom (a), nodules extracted from bottom in box corer (b), sorted nodules on measuring scale (c).

architecture itself, however, is extremely prolific and is also used as an important component in models such as recent breakthroughs in generative AI like Midjourney and Dall-E (Borji, 2022). The UNet network is a development of the autoencoder architecture and the convolutional network. The autoencoder architecture in its concept, implements the following idea. The input data (in this case, an RGB image) is gradually compressed by sending the information to fewer and fewer neurons until it reaches the so-called latent space, this process is called encoding. And then the course is reversed and the information compressed into the latent space is sent to more and more neurons, in a symmetrical way to the compression process, which is called decoding (Haque and Neubert, 2020). At the output, we expect such a network to return data (image) as similar as possible to the input image, so the network, in the hidden space, learns to compress the relevant features of the data (image). The similarity itself can be assessed by various measures, e.g. MSE.

The second "parent" of UNET networks is convolutional networks. The convolutional layer, makes the reasonable assumption that in image data it is the nearby pixels that are related to each other, forming so-called blobs, groups of pixels whose relationships can then be analyzed (Weng et al., 2019). This significantly reduces the size of the network, speeds up the learning time and bypasses the problems of, for example, fading or exploding gradients. The convolution is also associated with the operation of so-called pooling, which is a method (usually by taking the maximum value) of representing a group of pixels with a smaller number of variables/pixels and thus compression and the possibility of analysis at a higher level of abstraction (Hesamian et al., 2019).

The UNET network, in terms of shape, retains the visually striking feature of the autoencoder, that is, the form of an inverted hourglass (Fig. 7). On its input, there is an image, but on its output, we do not want to reproduce it, but we want to build a mask that will represent the classes into which we want to divide the input image.

The role of the researchers was to experimentally select the hyperparameters of the network, properly prepare the learning data, and analyze and respond to problems (under and overfitting) during learning.

The work used the Python programming language along with libraries to support scientific computing and data processing. Among them, it is necessary to highlight Tensorflow and Keras for building neural networks, Skimage for image processing and Numpy for storing images in the form of so-called arrays.

The data were randomly divided into 3 sets: test (10 %), validation (10 %) and learning (80 %). The validation set was used to determine quality metrics after each learning epoch.

The issue of assigning each pixel the appropriate class, in the case under analysis, nodule vs. background in computer vision is called semantic segmentation. It can be solved using classical computer vision techniques but due to variable lighting conditions between photos or the blurring of photos above technique could not provide satisfactory results.

The UNet output model was adapted to solve the problem of detecting nodules through a process of optimizing hyperparameters. To achieve optimal model performance, a grid search method was used, in which different values of key hyperparameters were carefully considered. A wide range of experiments were conducted, considering the following hyperparameters: optimizer, Input image size, Learning rate, network size and batch size.

3.4. Connected component analysis and watershed algorithm

Connected Component Analysis (CCA) is an image processing technique used to identify and isolate groups of connected pixels or regions in an image. It is an important step in image analysis that allows for the extraction and segmentation of different objects or areas in an image (Majanga and Viriri, 2021). The study used the OpenCV library in

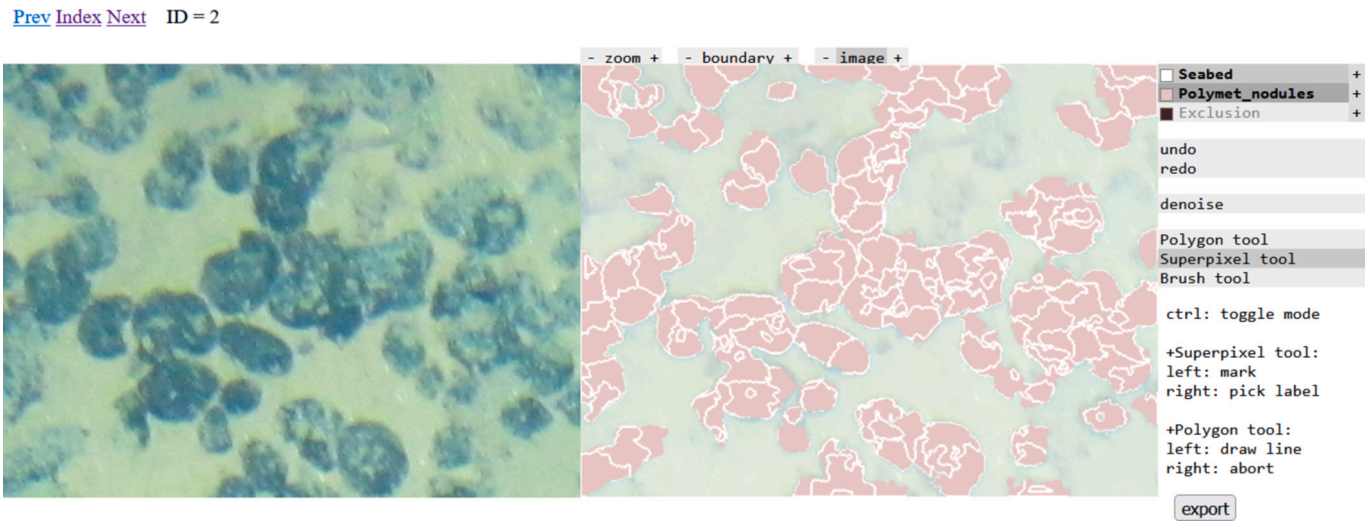

Fig. 4. Sample view of JS Segment Annotator.

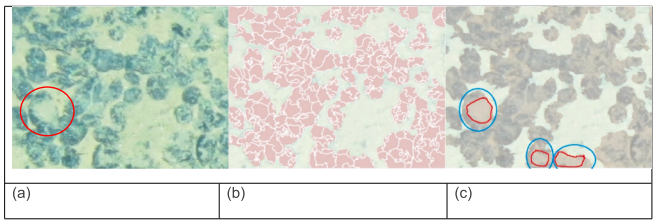

Fig. 5. Photo of nodules: (a), Photo with nodules labelled with SLIC super pixel algorithm: (b), Example of labelled buried nodules (blue polygon) with covering (red polygon): (c).

Python. CCA can have difficulty recognizing and analyzing complex, irregular shapes. If an object or region in an image has an unusual shape, this can lead to problems in identification and segmentation. In the case of closely spaced nodules that form a single region, CCA does not always separate regions into individual nodules. For this reason, a watershed algorithm was used for this type of object, which uses the topology of the image to identify boundaries between regions. The concept of the watershed can be expressed in terms of simulating flooding on a topographic surface (Amankwah and Aldrich, 2011). The algorithm determines the watersheds in an image and assigns each pixel the labels of the region to which it belongs. In the case of blocked nodules, it divides them into smaller corresponding images.

4. Results

The results presented in this report showcase a comprehensive analysis of polymetallic nodule abundance on the seabed, using advanced deep learning techniques. The data were gathered from a research cruise and subjected to both machine learning-based image segmentation and statistical modeling to estimate nodule abundance. The primary focus is on the application of a neural network model to

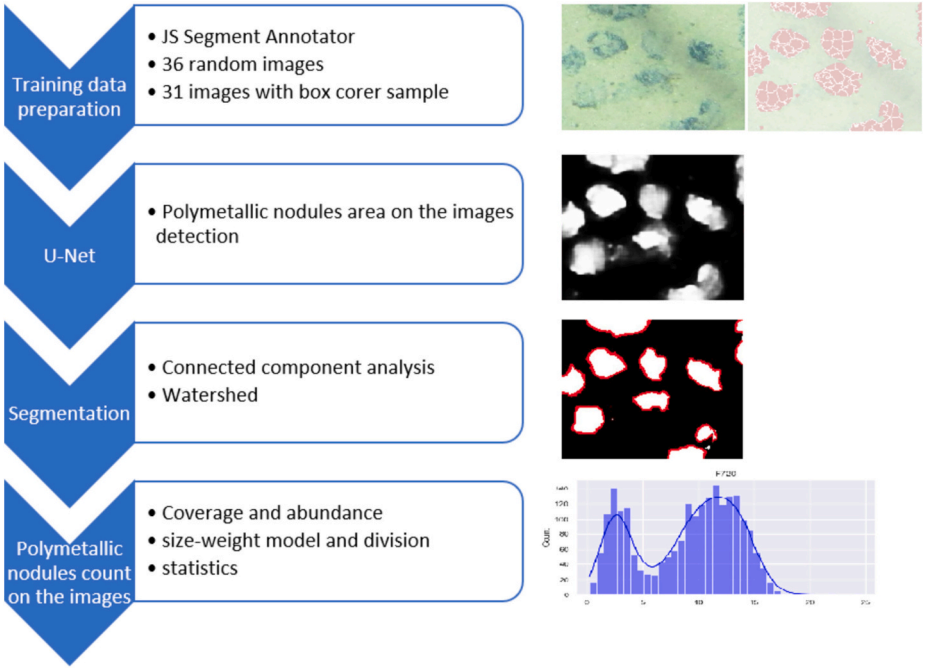

Fig. 6. Process flow chart of the nodule detection and segmentation.

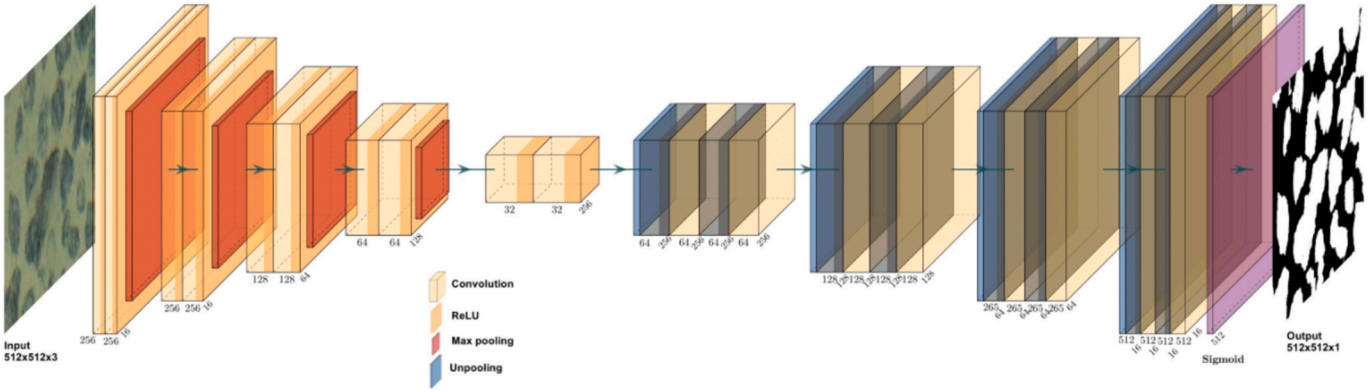

Fig. 7. The architecture of the UNet network applied in the research.

process images of the seabed, identifying nodules and distinguishing them from the surrounding seabed. Through various stages of image processing, including masking, segmentation, and binarization, the model successfully evaluated pixel probabilities for classifying nodules. The report also explores the learning curves of the model, discussing underfitting, overfitting, and the optimal balance between training and validation data. Additionally, a transition model was developed to convert the 2D coverage of nodules observed in the images to an estimate of mass per square meter. This process involved statistical evaluation of nodule size and weight distributions, leading to the construction of a power function that closely fits the gathered data. Visual data representations such as frequency histograms, box plots, and scatter plots are included to highlight the variability of nodule abundance across different survey lines.

4.1. Overview of image segmentation

The first column of (Fig. 8) shows excerpts from the raw, original images taken by the camera during the research cruise. In the second, the same photos, but with masks applied to them, were used during the learning and testing of the segmentation model. The third column contains the raw segmentation results coming out of the neural network. Attention should be paid to the fact that the result of the operation does not contain a binary image: black and white type, but an image with 256 shades from white to black. The value of each pixel was evaluated based on the probability of belonging to a class of nodules, and to a class of seabed. This raises interesting implications, which will be discussed later. Finally, the grayscale image was subjected to binarization and the operation of segmentation algorithms separating blocks of fractions into individual nodules. In the second row, column 3, the network differentiates (brightness of the image) the areas where the nodule is visible or partially covered. This effect is also evident in the other images. The network also can generalize even if a person in a given photo has not marked the nodule. This is evidenced by the last row, where a small nodule located in the middle right of the image was not marked by the expert, but the network detected it. Potentially, the biggest drawback is the transition to single instances of nodules from the entire nodule fraction. First, at the time of binarization, where we need to find the cutoff, and then during the segmentation algorithms, which sometimes result in clearly incorrect splits, as in the last row. Two possible research problems, currently being developed by the authors, arise here: the study of the impact of the threshold cutoff of the nodule-seabed boundary at different levels. Sometimes, as in row one, also for humans, the division is not obvious, but the proposed algorithm gives acceptable probable results. Before estimating the abundance of the deposit, the team conducted a statistical analysis of the results obtained. The evaluation was carried out at several levels: individual nodules, photos, specific photo survey lines where photos were taken, and the entire analyzed area.

4.2. Evaluation of model performance and learning curves

The selection of promising models was made by analyzing learning curves, showing how parameters such as cost function, accuracy or Intersection over Union (IoU) changed over successive epochs of model training for both learning and validation data. As a rule, these curves are highly correlated with each other, and it is usually sufficient to track one of them. This is a standard method used in machine learning (Tursyngaliyeva, 2019). Three example graphs are presented below (Fig. 9. Learning curves for training and validation data.). In the figure, we see a configuration where we have underfitting (Fig. 8: (a)). The result on the validation data is relatively weak compared to the result on the learning data. It can be speculated that the model (Q = 1) is relatively small and this causes it to be unable to learn better. Fig. 8: (b) shows the beginnings of overfitting. In this case, we can suspect that the model is too large, making it able to learn the data by heart. Because of this, the accuracy on the learning data increases and on the validation data decreases. The graph is cut because a technique called early stopping was used, i.e., if the model stops improving after a certain period of time, the experiment is stopped. This technique is used because the vast majority of experiments do not end with a satisfactory result, and the computational time is long and expensive. Fig. 8: (c) shows a run that we can consider desirable. The quality on both training and validation data is increasing, and there is not much discrepancy between them.

4.3. Mass estimation of nodules

The final determination of the mass of the concretions per square meter required the construction of the transition model from the 2D area occupied by the nodules to the mass. To do that the nodules retrieved from the bottom by the box corer were sorted with the use of a sieve every 20 mm and assigned to the following classes: 0–20 mm, 20–40 mm, 40–60 mm, 60–80 mm, 80–100 mm, 100–120 mm and >120 mm. Based on the data collected from the 48 sites, the average values of the weight of the nodules in each class were calculated, which allowed the creation of a model to recalculate further the nodules detected by the CNN. The model allows the conversion of the coverage of individual nodules calculated from the photo to mass. A power function with the formula was assumed

$$y = 2.6622x^{2.5911}$$

whose quality of model fit is described by the coefficient of determination R^2 of 0.9653.

This curve was obtained by averaging the mass of the nodules taken from the bottom and contained within the indicated mass ranges. The outlier for the largest mass is due to the fact that a small number of nodules of this size were extracted. However, as we will see in the results chapter, it applies to a marginal number of data. In addition to the

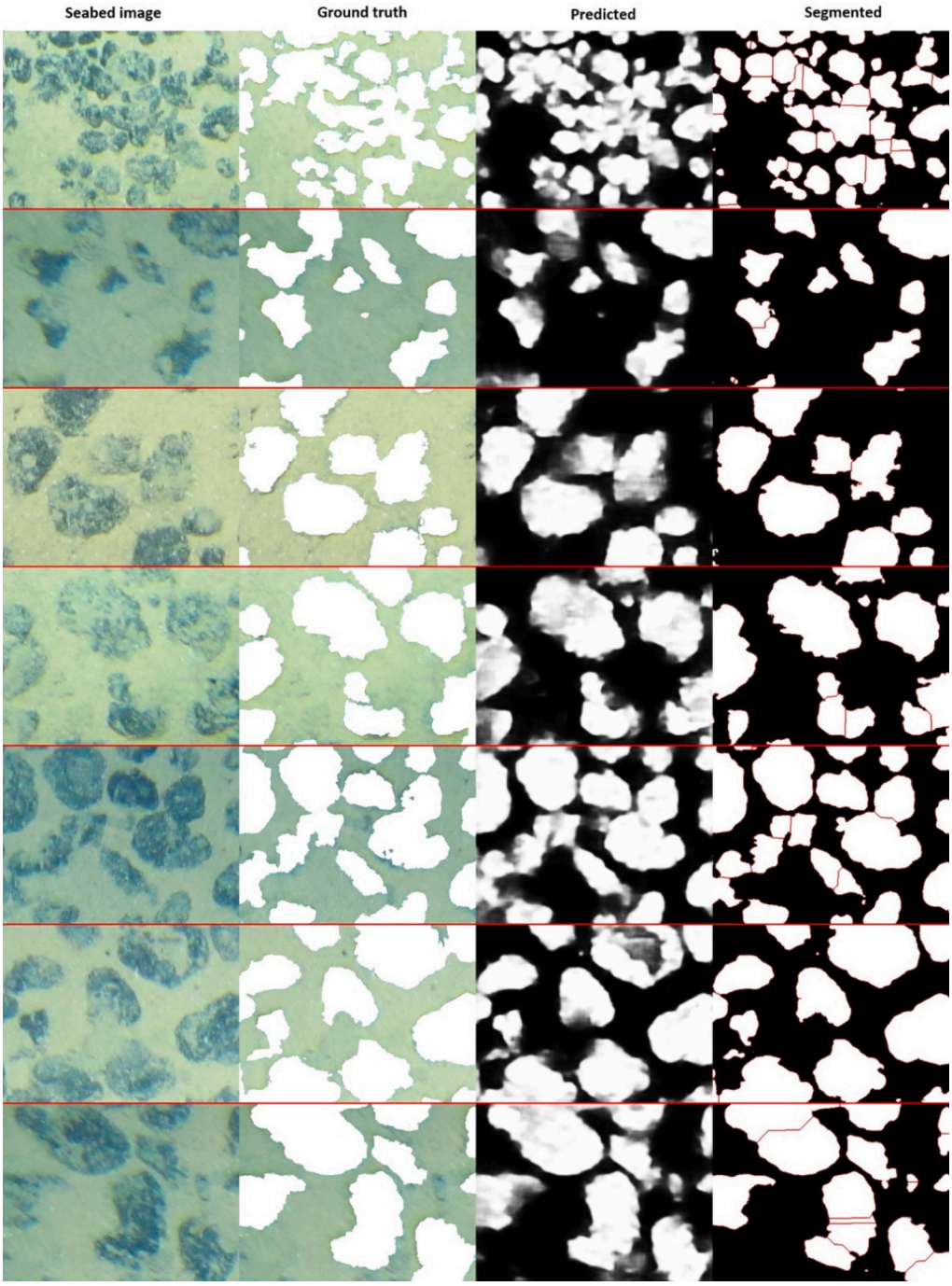

Fig. 8. Example results of detection and segmentation process.

exponential function, a very good fit can also be obtained using a polynomial of degree 3, which intuitively confirms the correctness of the estimate, since mass is proportional to the relatively constant density of the nodule and its volume, which, estimating the shape of the nodule using an ellipsoid, depends precisely on the third power of its linear size (Fig. 10).

4.4. Analysis of abundance variability

The histogram below is a graphical representation of the frequency distribution of the abundance for all processed image datasets with normal distribution density function fitted (Fig. 11). The abundance values are on the x-axis, and the frequency count is on the y-axis. The most common abundance values are between 6 and 10 kg/m^2. There are also a significant number with abundance values between 10 and 13 kg/m^2. There are fewer numbers with abundance values above 15 kg/m^2 and below 2 kg/m^2. The graph is also skewed to the right, meaning that there are more values with higher abundance than with lower. This suggests that distribution is dominated by high abundance on the seabed and it varies widely, but that most values have abundance between 2 and 13 kg/m^2.

For each 16 lines of the image series the box and whisker plot was generated (Fig. 12). The x-axis of the graph depicts the name of the image survey line, and the y-axis shows the abundance in kg/m^2. The supplied data as it was mentioned before come from two different areas of CCZ with different occurrences of nodules which is why plots can be

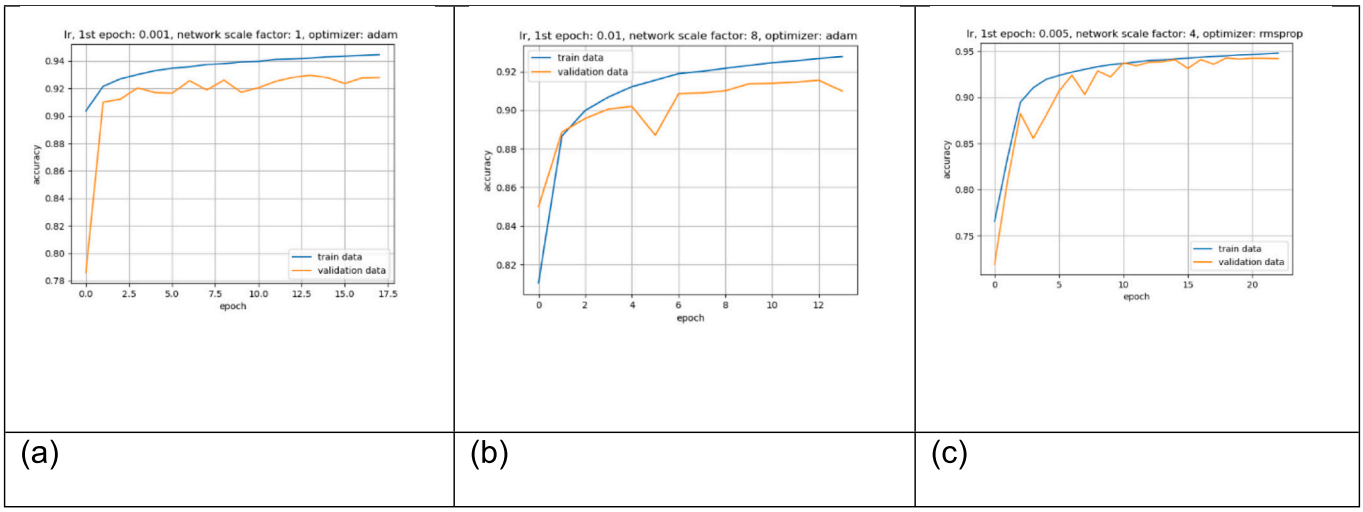

Fig. 9. Learning curves for training and validation data.

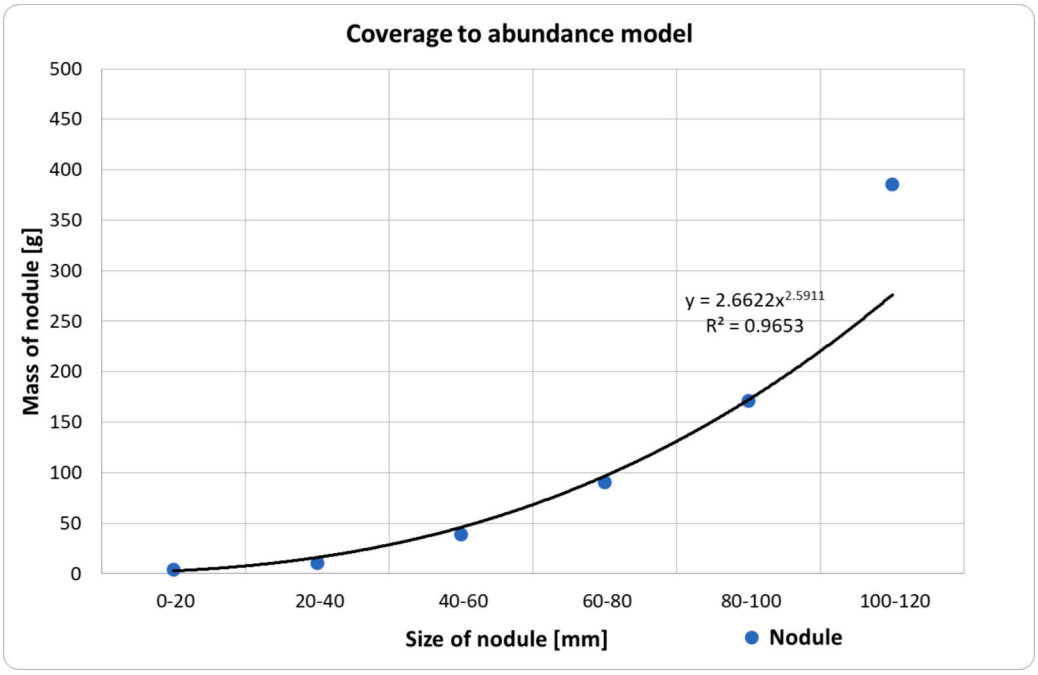

Fig. 10. Coverage to abundance model (CtA) fitted to box corer samples.

divided into two groups: 12 plots with the comparable median abundance oscillating around 8.0 kg/m^2 and 4 plots where the median abundance is significantly higher, around 10 kg/m^2. This means that half of the seabed photographs for first 12 lines have abundance values above 8.0 kg/m^2 and half have abundance values below 8,0 kg/m^2. The next 4 lines have abundance values above 10.0 kg/m^2 and half have abundance values below 10.0 kg/m^2. For these groups respectively the quartiles show that the middle 50 % of the data is between 7.5–8.5 and 5–12 kg/m^2. The whiskers inform that the range of the data is from 2.5 to 15 for first 12 image lines and 0–25 kg/m^2 for the remaining 4 lines.

There are many more outliers in the data for the first group of lines, and few for the second group. There are a few outliers in the data, with abundance values above 25 kg/m^2. However, these outliers are relatively rare. The majority of the data points in the first group, in the interquartile range (IQR), fall close to the median indicating that the abundance of polymetallic nodules is relatively consistent across most seabed photographs. For the second group situation is different IQR is wider, and values are not so closely scattered around the median value.

It can be concluded that the study area is characterized by a relatively stable distribution of nodule abundance. Both in terms of median mass density per area and IQR. Instead, significantly higher IQR is shown by lines F720, 721, 722P and 725P, but they do not lie within the study area. They were added to indicate heterogeneity among marine parcels and nodule deposits in different areas.

The calculated mean value of abundance for all RGB images along the lines illustrates in the bar graph (Fig. 13). The x-axis of the graph shows the name of the image survey line, and the y-axis shows the mean abundance in kg/m^2. The overall trend is staying at a similar level with no clear ups and downs for the whole area H22NE. The value of the mean for all lines is in the range of 8 to 9 kg/m^2. Even for the 4 lines outside the area H22NE the mean value is within this range even though the modes and medians were different.

The maximum values are characterized by a much greater variation than the average values and are arranged in the range from 18 to 25 kg/

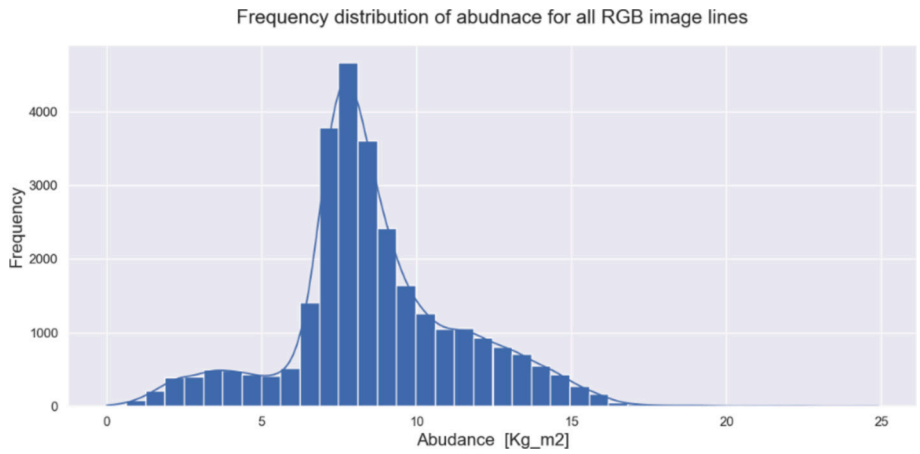

Fig. 11. Frequency distribution of abundance for all RGB images processed.

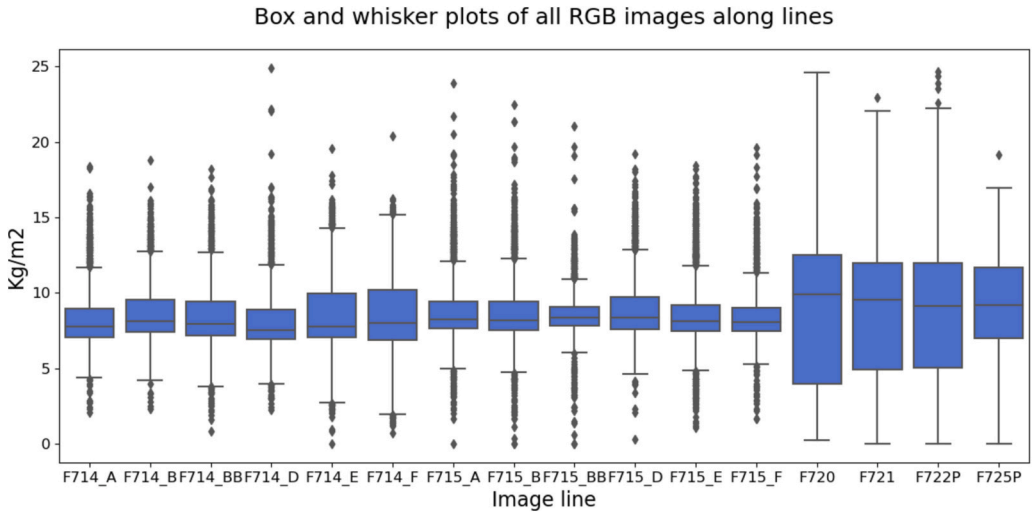

Fig. 12. Box and whisker plots of all RGB images processed.

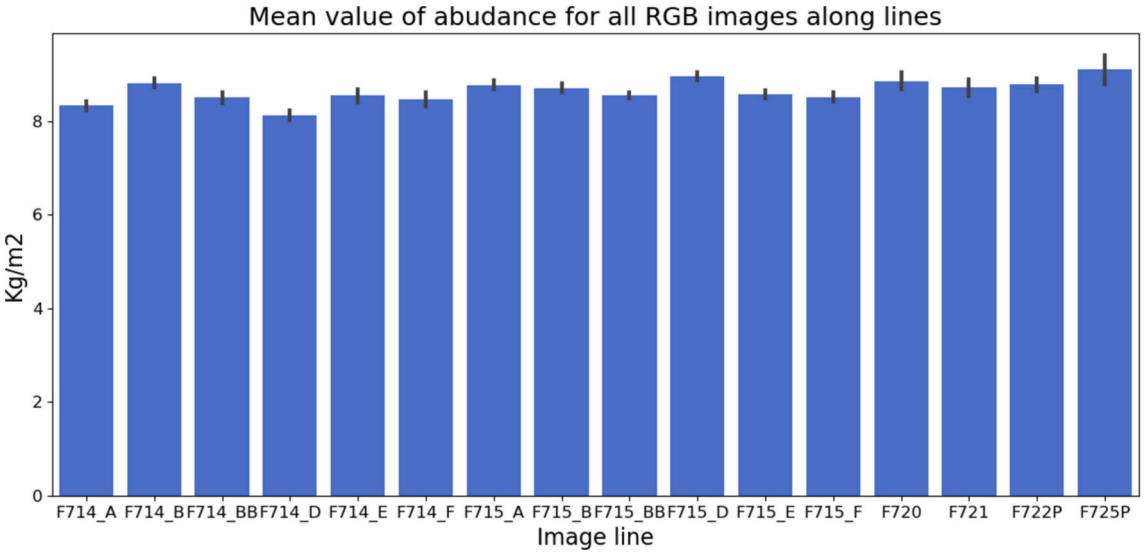

Fig. 13. Mean values of abundance for all RGB images along all survey lines.

m^2 (Fig. 14). Here it is difficult to find relations of values with the location of the survey line in the area. The minimum values for the individual survey lines, on the other hand, are even less varied than the maximum values and range from 0 to 2.5 kg/m^2 (Fig. 15). Half of the lines have minimum values >0, which means that a certain number of nodules were detected in all photographs along these lines, and no areas without their occurrence were identified.

A provided strip plot graph as a complementary scatter plot visualizes the distribution of abundance across different survey lines (Fig. 16). It instead of showing the median, quartiles, and whiskers shows each individual data point represented by dots. There is a general trend the data for the H22NE area has a lower abundance and narrower range. Abundance values are not so evenly distributed as for the data from outside H22NE. This could be due to a number of factors, such as changes in the seabed type, seabed sediments on top of nodules, or other environmental conditions.

Data determined from analysis of images of seabed taken along survey lines in the area from west to east direction provide information on the variability of the calculated abundance along the direction of the survey lines. The resolution of data is very high. Every 5–10 m there is one image available. At this stage of research, we consider it is possible to infer estimated abundance for the entire area, if the data can be analyzed collectively. This however requires further implementation of statistical methods relevant to resource estimations, such as kriging or similar methods, such that the estimation could be confirmed by a competent person according to a geological standard.

An aggregated abundance value was determined for each survey line. It is shaped between 5000 kg for line F725P and 26,000 for line F722P (Fig. 17).

4.5. Analysis of the seafloor area covered by the images

The sum of the area of the bottom covered by the images in each survey line with a similar distribution of the size of the coverage area for a single image depends on the number of images in the line. The number of photos in a line, on the other hand, is derived from the length of the line assuming a constant interval between successive photos (Fig. 18).

The distribution of values for the area of the bottom covered by a single image in each survey line is shown in Fig. 19.

Most of the strips, the IQR is similar, ranging from 3.5 to 4.25 m^2 with a median of about 3.75 m^2. This means that good control of the height of the camera above the bottom was maintained at the time the images were taken, with a similar standard deviation of about 0.6 m^2. The distribution of the calculated area covered by the images on survey line F715_A and 715_B has a lower median, but similar IQR. In contrast, the F715_BB line shows a much lower median and narrower IQR range. The reason for this is the closer position of the camera to the bottom during towing.

The total area of coverage in each line varies between 5000 m^2 and 10,500 m^2 (Fig. 24). The calculated summed bottom coverage area for all lines was 110,337 m^2. In comparison, the area of bottom coverage by box corer at the time of sampling in the H22NE area was 7.75 m^2.

This allows to conclude that the use of vision methods in estimating the abundance of nodules in terms of the size of the sampling area, in the set of data we have, has significantly greater potential than direct samples (Fig. 20).

The weight of nodules for sorted values of nodule sizes on analyzed profiles is presented in (Fig. 21). There is a significant difference between the profiles inside the H22 NE area and the profiles from other places of the exploration area. This difference confirms earlier observations about the variability of the type of nodules characteristic of a given area. These differences were recognized by the neural network, resulting in completely different weight characteristics. Of course, the nodules of the same size have the same masses, but in different areas there are different numbers of smaller nodules and different larger nodules. It is visible that in areas outside H22NE there are a greater number of large nodules and this gives a higher total weight for these groups. In the H22 NE area there is a greater number of smaller nodules and they determine the weight on the profiles from this area.

5. Discussion

The results of this study provide a significant advancement in the estimation of polymetallic nodule abundance using deep learning models applied to seafloor imagery. By leveraging the UNet convolutional neural network framework, we were able to automate the detection and quantification of nodules, demonstrating substantial improvements in speed and efficiency compared to traditional methods such as direct sampling and acoustic imagery. The study successfully processed over 30,000 seabed photographs in under 10 h, a vast improvement in time efficiency, making this approach highly scalable for large exploration areas like the Clarion-Clipperton Zone (CCZ). The findings from this study not only contribute to the ongoing development of more efficient and scalable methods for deep-sea resource assessment but also provide valuable insights for future exploration and potential exploitation of these resources. The ability to accurately map nodule distribution and abundance is essential for evaluating the feasibility of deep-sea mining operations and for developing strategies to minimize

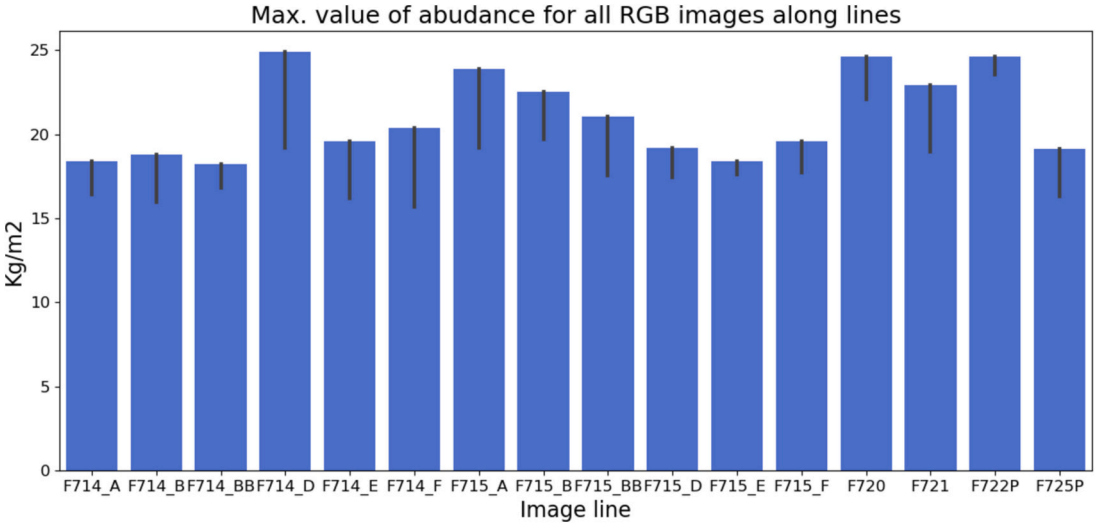

Fig. 14. Maximum values of abundance for all survey lines of RGB images.

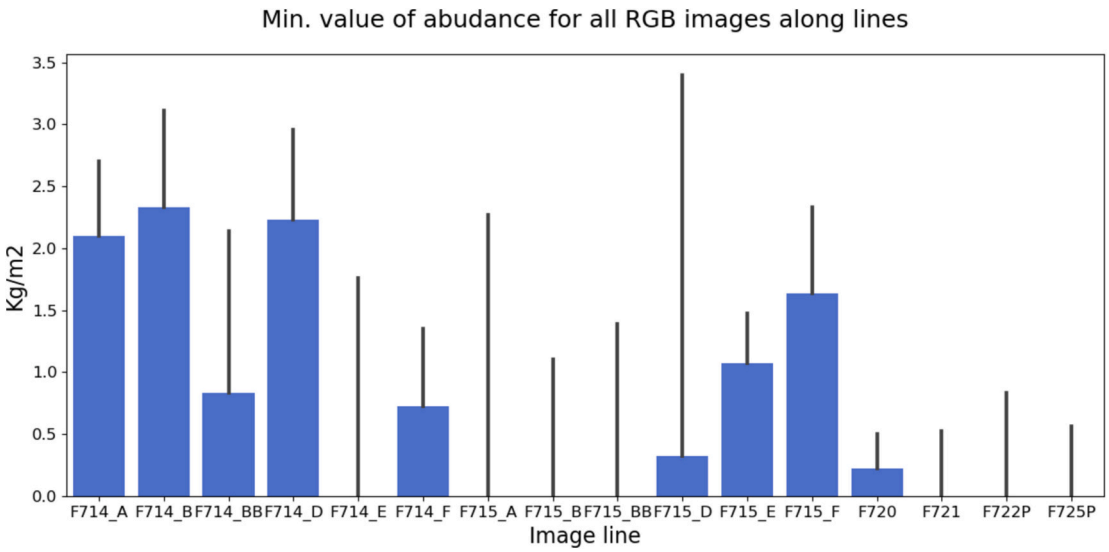

Fig. 15. Minimum values of abundance for all survey lines of RGB images.

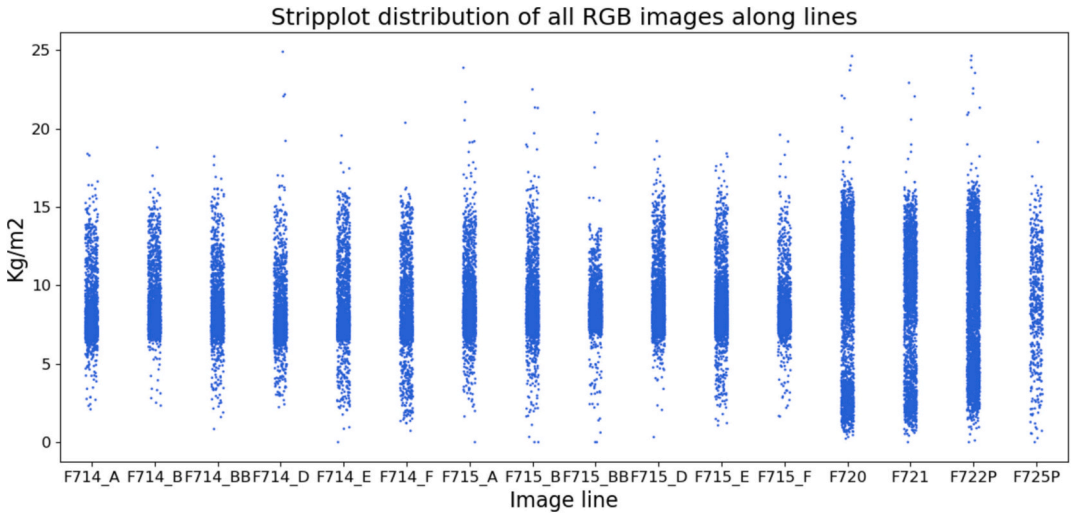

Fig. 16. Strip plot distribution of all RGB images for all survey lines.

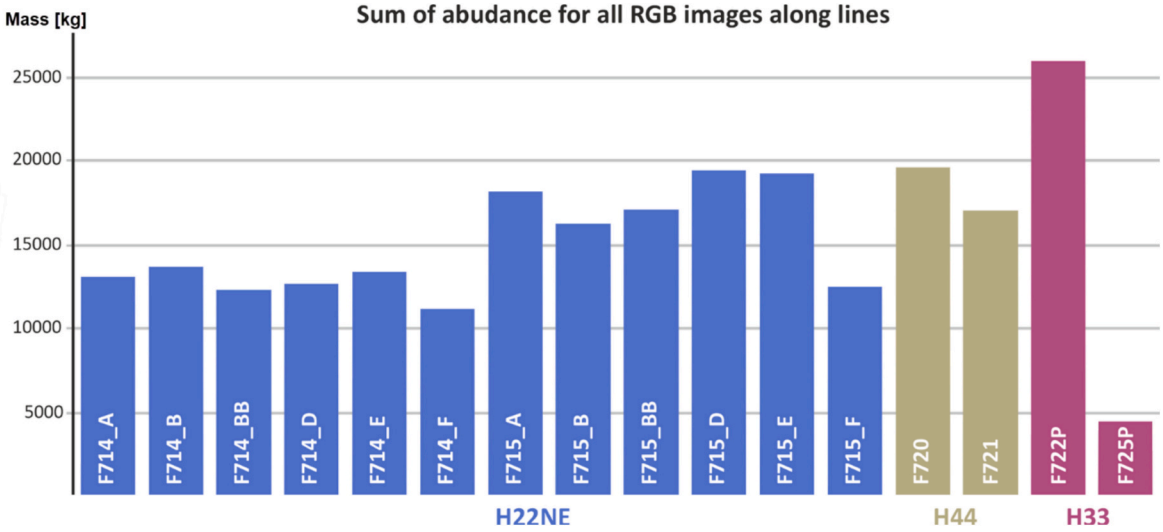

Fig. 17. Summarized abundance for each photo survey lines in all analyzed areas.

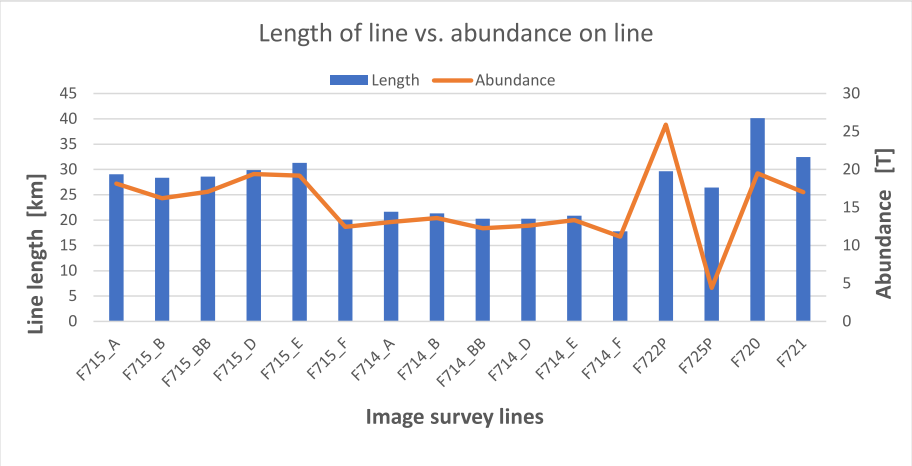

Fig. 18. Length of photo survey line and determined abundance.

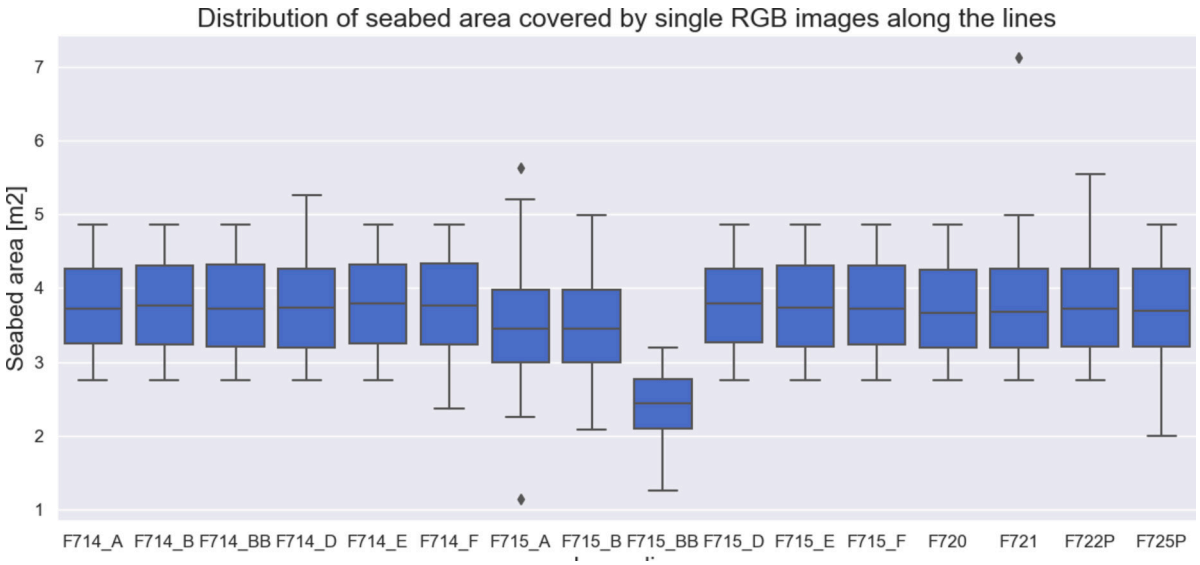

Fig. 19. Distribution of seabed area covered by single image along the survey lines.

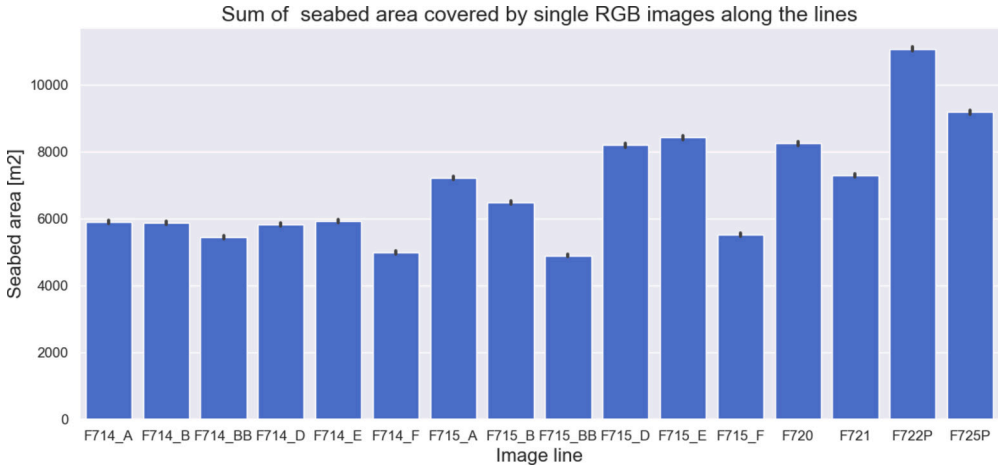

Fig. 20. The sum of seabed area covered by single RGB images in each line.

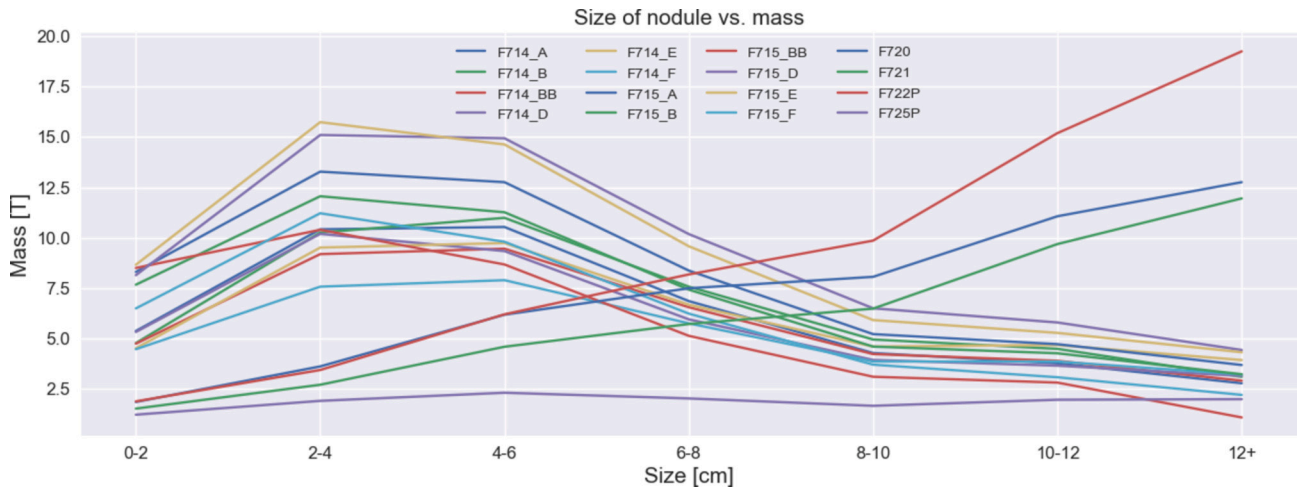

Fig. 21. Total mass of nodule for sorted values of nodules size on analyzed survey line.

environmental impact.

Nevertheless, challenges remain, particularly in terms of the diversity of data needed to train models. Current deep learning models are often trained on limited datasets, which may not fully account for the variability in environmental conditions, sediment types, and nodule morphologies across different regions of the ocean floor.

One of the key findings is the model's ability to estimate nodule abundance with reasonable accuracy. The abundance estimates derived from the deep learning model, which ranged between 6 and 25 kg/m^2, are consistent with previously reported values for highly prospective mining areas in the CCZ (Rühlemann et al., 2011; Ellefmo and Kuhn, 2021; Mucha and Wasilewska-Błaszczyk, 2020; Wasilewska-Błaszczyk and Mucha, 2021). Although the model underestimates true abundance in certain cases compared to traditional samples (due to challenges like nodules being buried under sediment or image quality degradation), it nonetheless provides a reliable estimation tool for preliminary resource assessment. The majority of nodules are found at the surface but exploration campaigns and nodules sampling in Clarion Clipperton, carried out by IOM or other ISA contractors, e.g. (Kotlinski and Stoyanova, 2007; Yang et al., 2024) has revealed that there can be some nodules buried at the deposit depths of range from several centimeters to 0.5 m. They were as well studied from the geotechnical and mineralogical point of view (Fan et al., 2024). Buried nodules and/or their spatial distribution can only be identified using physical sampler, e.g. box corer or grab sampler. There aren't any systematic and statistically valid comparisons between data (nodule abundance) that were obtained from cruise for buried nodules and how they can be compared to the abundance of surface nodules but it is said that in some places locally can be up to 25 % more nodules buried at depths of 5–40 cm (Parianos et al., 2021).

This pattern is however random, local, and would require additional investigations during sampling. There were places where no buried nodules were collected at all. Buried polymetallic nodules are not considered to be included in the estimation of resources (Parianos et al., 2021) because of the three most important reasons:

- accessibility: Buried nodules are covered by thick layer of sediment and are therefore harder to access than those on the seafloor surface. The technology and methods required to recover buried nodules are more complex, expensive, and less efficient compared to those on the surface.
- uncertain quantity and quality: The exact quantity and quality of buried nodules are difficult to ascertain, especially for imaging methodology. Their location, depth of burial, and concentration within the sediment are uncertain, making it challenging to accurately estimate their potential as a resource and to identify them during extraction.
- environmental impact: Extracting buried nodules would likely involve more intrusive and damaging processes than collecting surface nodules, potentially causing significant disruption to the marine environment. Much more sediment is to be stripped if buried nodules are to be considered for mining. This includes disturbing the seabed habitat, which could have long-lasting ecological consequences.

Given the aforementioned factors, the authors believe that excluding buried nodules from the resource calculation does not lead to an underestimation of the resource estimates. This is because buried nodules are currently inaccessible due to the existing environmental and depositional conditions. Consequently, it is challenging to categorize them as a resource at all currently.

Another limitation may lie in the two-step segmentation process, where first, the image is divided into nodules and the background, and then the nodule fraction is further segmented into individual nodules. While effective, this process introduces potential errors, particularly in accurately delineating individual nodules in densely packed areas. Future work could focus on implementing instance or panoptic segmentation models, which might offer more precise nodule identification by treating each nodule as a separate instance from the outset.

Polymetallic nodules in the Clarion-Clipperton Zone (CCZ) typically exhibit a rounded to elongated, irregular shape. This makes it difficult to determine the exact size of the single. These nodules are often described as potato-like in appearance, with smooth or slightly rough surfaces. Their size can vary significantly, ranging from a few centimeters to over 10 cm in diameter. The shape and size of the nodules are influenced by the growth process, which involves the precipitation of metal layers over time around a core, usually of biological origin or a fragment of rock (Hein et al., 2013; Sharma et al., 2010). The paper assumes that the size of the nodules and their size class membership can be determined based on the so-called soft sieve, which is software equivalent to a physical sieve used in the process of nodule sorting when derived from the bottom. The sorting of nodules is based on their movement over the sieve, with nodule particles larger than the sieve mesh size moving freely over the sieve surface and forming a larger fraction, and smaller particles passing through the mesh and being collected a smaller fraction. This means that the more irregular (elongated) the shape, the more likely it is that nodules whose diameter is larger than the sieve mesh can pass through the mesh. It may propagate on inaccuracies in mass determination.

6. Conclusions

Utilizing deep learning techniques for nodule detection and segmentation in seafloor images enabled the estimation of polymetallic nodule abundance with promising accuracy. The deep learning model successfully identified and quantified nodules, yielding a mean abundance of 8.5 kg/m^2 and a maximum abundance of 25 kg/m^2. The abundance estimates exhibited spatial variability along the survey line, highlighting the heterogeneous distribution of nodules on the seafloor. The study's findings also demonstrated that the deep learning model could effectively handle images with minimum abundance values greater than zero. To achieve this, a coverage-to-abundance model based on seabed samples was developed and integrated with the deep learning model. This integrated approach facilitated the estimation of abundance across the entire survey line, including areas with varying nodule densities. Integrating deep learning with seafloor imagery and traditional sampling methods offers a comprehensive and robust approach to assessing polymetallic nodule resources in the deep sea. This methodology complements the need for extensive physical sampling, promoting a more sustainable and efficient exploration process. It should emphasize that only visible nodules or part of nodules were evaluated in the process. It means the overall method underestimates the real abundance. Despite this, the solution introduces a great deal of valuable information in deposit estimation and mining planning. It provides an opportunity to assess coverage variability and granulation variation and to identify areas with high or very high concentrations of nodules.

Also, information about the absence of visible nodules in the images, in the context of geological settings and the possibility of their occurrence under the sedimentary layer, however, may indicate a high probability of their absence or low, economically insignificant abundance in the area.

The deep learning approach provides several advantages over earlier methods:

- Scalability: Once trained, deep learning models can process large datasets of seafloor photographs rapidly, enabling faster analysis over vast regions compared to manual or semi-automated methods.
- Automation: Reducing the reliance on human experts for nodule identification reduces subjectivity and labour-intensive manual efforts.
- Improved Accuracy: Deep learning models can integrate multi-modal data sources (e.g., image data with sonar or other sensor data), improving the robustness of abundance predictions.

Further research should focus on enhancing the generalizability of the deep learning model by incorporating a broader range of seabed environments, nodule morphologies, and illumination conditions. Additionally, investigating the applicability of the deep learning model to different seabed survey systems will broaden its potential for widespread adoption.

While current models rely heavily on supervised learning, the future may see an increase in self-supervised or unsupervised learning techniques. These models can learn to detect patterns in seafloor data with minimal labelled examples, which is particularly beneficial in deep-sea environments where labelled datasets are often scarce. By pre-training models on larger, more diverse datasets and then fine-tuning them on specific regions, researchers can increase both the accuracy and efficiency of nodule abundance estimations. With advancements in underwater robotics and autonomous vehicles, there is potential for real-time nodule detection and estimation using deep learning algorithms. These systems could continuously capture and analyze seafloor images, providing up-to-date information on nodule abundance for mining operations.

In conclusion, applying deep learning to seafloor images, combined with traditional sampling methods, has proven to be an effective tool for mapping polymetallic nodule abundance and distribution. This methodology holds significant potential for advancing deep-sea exploration and resource management practices, paving the way for sustainable and responsible resource utilization.

CRediT authorship contribution statement

Arkadiusz Tomczak: Writing – review & editing, Writing – original draft, Visualization, Validation, Supervision, Resources, Project administration, Methodology, Investigation, Formal analysis, Data curation, Conceptualization. **Tomasz Kogut:** Writing – original draft, Methodology, Investigation, Formal analysis, Data curation, Conceptualization. **Karol Kabała:** Writing – original draft, Visualization, Methodology, Investigation, Formal analysis, Data curation. **Tomasz Abramowski:** Writing – review & editing, Supervision, Resources, Methodology. **Jakub Ciążela:** Writing – review & editing, Methodology, Investigation. **Andrzej Giza:** Writing – review & editing, Visualization.

Declaration of competing interest

The authors declare that they have no known competing financial interests or personal relationships that could have appeared to influence the work reported in this paper.

Appendix A. Supplementary data

Supplementary data to this article can be found online at https://doi.org/10.1016/j.scitotenv.2024.177225.

Data availability

Data will be made available on request.

References

Alevizos, E., Schoening, T., Koeser, K., Snellen, M., Greinert, J., 2018. Quantification of the Fine-Scale Distribution of Mn-Nodules: Insights From AUV Multi-Beam and Optical Imagery Data Fusion. https://doi.org/10.5194/bg-2018-60.

Amankwah, A., Aldrich, C., 2011. Automatic Estimation of Rock Particulate Size on Conveyer Belt Using Image Analysis. https://doi.org/10.1117/12.913415 (82851E).

Borji, A., 2022. Generated Faces in the Wild: Quantitative Comparison of Stable Diffusion, Midjourney and DALL-E 2.

Carraro, A., Sozzi, M., Marinello, F., 2023. The Segment Anything Model (SAM) for accelerating the smart farming revolution. Smart Agricultural Technology 6, 100367. https://doi.org/10.1016/j.atech.2023.100367.

Darapaneni, N., Raj, P., Paduri, A.R., Anand, E., Rajarathinam, K., Eapen, P.T., et al., 2021. Autonomous Car Driving Using Deep Learning, pp. 29–33. https://doi.org/10.1109/ICSCCC51823.2021.9478090.

Dong, L., Wang, H., Song, W., Xia, J., Liu, T., 2021. Deep sea nodule mineral image segmentation algorithm based on Mask R-CNN. In: Proceedings of the ACM Turing Award Celebration Conference—China (ACM TURC 2021), pp. 278–284 (30 July–1 August).

Ellefmo, S.L., Kuhn, T., 2021. Application of soft data in nodule resource estimation. Nat. Resour. Res. 30 (2), 1069–1091. https://doi.org/10.1007/s11053-020-09777-2.

Fan, Z., Li, X., Li, Z., Ma, W., Zhu, Z., Li, J., et al., 2024. Geochemical behavior of shallow buried nodules from Clarion–Clipperton Fracture Zone in the east Pacific: a LA-ICP-MS mapping analysis perspective. Minerals 14 (1), 80. https://doi.org/10.3390/min14010080.

Felix, D., 1980. Some problems in making nodule abudance estimates from seafloor photographs. Mar. Mining 2, 293–302.

Gazis, I.-Z., Schoening, T., Alevizos, E., Greinert, J., 2018. Quantitative mapping and predictive modeling of Mn nodules' distribution from hydroacoustic and optical AUV data linked by random forests machine learning. Biogeosciences 15 (23), 7347–7377. https://doi.org/10.5194/bg-15-7347-2018.

Hade, M., Yuliang, L., Hongzhe, Y., Cheng, Q., Jing, X., 2020. Image processing of manganese nodules based on background gray value calculation. Computers, Materials & Continua 65 (1), 511–527. https://doi.org/10.32604/cmc.2020.09841.

Haque, I.R.I., Neubert, J., 2020. Deep learning approaches to biomedical image segmentation. Informatics in Medicine Unlocked 18, 100297. https://doi.org/10.1016/j.imu.2020.100297.

He, H., Xu, H., Zhang, Y., Gao, K., Li, H., Ma, L., et al., 2022. Mask R-CNN based automated identification and extraction of oil well sites. Int. J. Appl. Earth Obs. Geoinf. 112, 102875. https://doi.org/10.1016/j.jag.2022.102875.

Hein, J.R., Mizell, K., Koschinsky, A., Conrad, T.A., 2013. Deep-ocean mineral deposits as a source of critical metals for high- and green-technology applications: comparison

with land-based resources. Ore Geol. Rev. 51, 1–14. https://doi.org/10.1016/j.oregeorev.2012.12.001.
Hein, J.R., Koschinsky, A., Kuhn, T., 2020. Deep-ocean polymetallic nodules as a resource for critical materials. Nat Rev Earth Environ 1 (3), 158–169. https://doi.org/10.1038/s43017-020-0027-0.
Hesamian, M.H., Jia, W., He, X., Kennedy, P., 2019. Deep learning techniques for medical image segmentation: achievements and challenges. J. Digit. Imaging 32 (4), 582–596. https://doi.org/10.1007/s10278-019-00227-x.
International Seabed Authority, 2018. Exploration licence map. https://iom.gov.pl/exploration-licence/.
Karimpouli, S., Tahmasebi, P., 2019. Segmentation of digital rock images using deep convolutional autoencoder networks. Comput. Geosci. 126, 142–150. https://doi.org/10.1016/j.cageo.2019.02.003.
Kotlinski, R., Stoyanova, V., 2007. Buried and Surface Polymetallic Nodules Distribution in the Eastern Clarion Clipperton Zone: Main Distinction and Similarities, pp. 67–74.
Kuhn, T., Rühlemann, C., 2021. Exploration of Polymetallic Nodules and Resource Assessment: A Case Study From the German Contract Area in the Clarion-Clipperton Zone of the Tropical Northeast Pacific.
Kuhn, Thomas, Rühlemann, Carsten, Wiedicke-Hombach, Michael, 2020. Development of Methods and Equipment for the Exploration of Manganese Nodules in the German License Area in the Central Equatorial Pacific.
Liu, Y., Zhang, Z., Liu, X., Wang, L., Xia, X., 2021. Efficient image segmentation based on deep learning for mineral image classification. Adv. Powder Technol. 32 (10), 3885–3903. https://doi.org/10.1016/j.apt.2021.08.038.
Maciąg, Ł., Zawadzki, D., Kozub-Budzyń, G.A., Piestrzyński, A., Kotliński, R.A., Wróbel, R.J., 2019. Mineralogy of cobalt-rich ferromanganese crusts from the Perth Abyssal Plain (E Indian Ocean). Minerals 9 (2), 84. https://doi.org/10.3390/min9020084.
Majanga, V., Viriri, S., 2021. Dental images' segmentation using threshold connected component analysis. Comput. Intell. Neurosci. 2021, 2921508. https://doi.org/10.1155/2021/2921508.
Milinovic, J., Rodrigues, F.J.L., Barriga, F.J.A.S., Murton, B.J., 2021. Ocean-floor sediments as a resource of rare earth elements: an overview of recently studied sites. Minerals 11 (2), 142. https://doi.org/10.3390/min11020142.
Miller, K.A., Thompson, K.F., Johnston, P., Santillo, D., 2018. An overview of seabed mining including the current state of development, environmental impacts, and knowledge gaps. Front. Mar. Sci. 4. https://doi.org/10.3389/fmars.2017.00418.
Mucha, J., Wasilewska-Błaszczyk, M., 2020. Estimation Accuracy and Classification of Polymetallic Nodule Resources Based on Classical Sampling Supported by Seafloor Photography (Pacific Ocean, Clarion-Clipperton Fracture Zone, IOM Area).
Mucha, J., Kotliński, R., Wasilewska-Błaszczyk, M., 2011. Metodyka szacowania parametrów zasobowych z^{3}ó¿ konkrecji polimetalicznych w obszarze Interoceanmetal na Pacyfiku. Zeszyty Naukowe (81).
Munawar, H.S., Hammad, A.W.A., Waller, S.T., Shahzad, D., Islam, M.R., 2023. Road network detection from aerial imagery of urban areas using deep ResUNet in combination with the B-snake algorithm. Hum-Cent Intell Syst 3 (1), 37–46. https://doi.org/10.1007/s44230-023-00015-5.
Pan, Z., Xu, J., Guo, Y., Hu, Y., Wang, G., 2020. Deep learning segmentation and classification for urban village using a worldview satellite image based on U-Net. Remote Sens. (Basel) 12 (10), 1574. https://doi.org/10.3390/rs12101574.
Parianos, J., Lipton, I., Nimmo, M., 2021. Aspects of estimation and reporting of mineral resources of seabed polymetallic nodules: a contemporaneous case study. Minerals 11 (2), 200. https://doi.org/10.3390/min11020200.
Peukert, A., Schoening, T., Alevizos, E., Köser, K., Kwasnitschka, T., Greinert, J., 2018. Understanding Mn-nodule distribution and evaluation of related deep-sea mining impacts using AUV-based hydroacoustic and optical data. Biogeosciences 15 (8), 2525–2549. https://doi.org/10.5194/bg-15-2525-2018.
Ronneberger, O., Fischer, P., Brox, T., n.d. U-Net: Convolutional Networks for Biomedical Image Segmentation.
Rühlemann, Carsten, Kuhn, Thomas, Wiedicke, Michael, Kasten, Sabine, Mewes, Konstantin, Picard, Aude, 2011. Current status of manganese nodule exploration in the German license area. In: Proceedings of the Ninth (2011) ISOPE Ocean Mining Symposium.
Sakellariadou, F., Gonzalez, F.J., Hein, J.R., Rincón-Tomás, B., Arvanitidis, N., Kuhn, T., 2022. Seabed mining and blue growth: exploring the potential of marine mineral deposits as a sustainable source of rare earth elements (MaREEs) (IUPAC Technical Report). Pure Appl. Chem. 94 (3), 329–351. https://doi.org/10.1515/pac-2021-0325.
Schoening, T., Kuhn, T., Jones, D.O., Simon-Lledo, E., Nattkemper, T.W., 2016. Fully automated image segmentation for benthic resource assessment of poly-metallic nodules. Methods in Oceanography 15-16, 78–89. https://doi.org/10.1016/j.mio.2016.04.002.
Serikawa, S., Lu, H., 2014. Underwater image dehazing using joint trilateral filter. Computers & Electrical Engineering 40 (1), 41–50. https://doi.org/10.1016/j.compeleceng.2013.10.016.
Shao, M., Song, W., Zhao, X., 2023. Polymetallic nodule resource assessment of seabed photography based on denoising diffusion probabilistic models. JMSE 11 (8), 1494. https://doi.org/10.3390/jmse11081494.
Sharma, R., Sankar, S.J., Samanta, S., Sardar, A.A., Gracious, D., 2010. Image analysis of seafloor photographs for estimation of deep-sea minerals. Geo-Mar. Lett. 30 (6), 617–626. https://doi.org/10.1007/s00367-010-0205-z.
Sharma, R., Khadge, N.H., Jai Sankar, S., 2013. Assessing the distribution and abundance of seabed minerals from seafloor photographic data in the Central Indian Ocean Basin. Int. J. Remote Sens. 34 (5), 1691–1706. https://doi.org/10.1080/01431161.2012.725485.
Song, W., Zheng, N., Liu, X., Qiu, L., Zheng, R., 2019. An improved U-Net convolutional networks for seabed mineral image segmentation. IEEE Access 7, 82744–82752. https://doi.org/10.1109/ACCESS.2019.2923753.
Tsune, A., 2021. Quantitative expression of the burial phenomenon of deep seafloor manganese nodules. Minerals 11 (2), 227. https://doi.org/10.3390/min11020227.
Tsune, Akira, Okazaki, Masatsugu, 2014. Some Considerations About Image Analysis of Seafloor Photographs for Better Estimation of Parameters of Polymetallic Nodule Distribution.
Tursyngaliyeva, Assem, 2019. Deep Learning for Medical Image Segmentation: Pneumonia Detection. https://doi.org/10.13140/RG.2.2.12773.14560.
Volkmann, S.E., Kuhn, T., Lehnen, F., 2018. A comprehensive approach for a techno-economic assessment of nodule mining in the deep sea. Miner. Econ. 31 (3), 319–336. https://doi.org/10.1007/s13563-018-0143-1.
Wasilewska-Błaszczyk, M., Mucha, J., 2020. Possibilities and limitations of the use of seafloor photographs for estimating polymetallic nodule resources—case study from IOM area, Pacific Ocean. Minerals 10 (12), 1123. https://doi.org/10.3390/min10121123.
Wasilewska-Błaszczyk, M., Mucha, J., 2021. Application of General Linear Models (GLM) to assess nodule abundance based on a photographic survey (case study from IOM Area, Pacific Ocean). Minerals 11 (4), 427. https://doi.org/10.3390/min11040427.
Weaver, P., Aguzzi, J., Boschen-Rose, R.E., Colaço, A., de Stigter, H., Gollner, S., et al., 2022. Assessing plume impacts caused by polymetallic nodule mining vehicles. Mar. Policy 139, 105011. https://doi.org/10.1016/j.marpol.2022.105011.
Weng, Y., Zhou, T., Li, Y., Qiu, X., 2019. NAS-Unet: neural architecture search for medical image segmentation. IEEE Access 7, 44247–44257. https://doi.org/10.1109/ACCESS.2019.2908991.
Wong, Liang Jie, Kalyan, Bharath, Chitre, Mandar, Vishnu, Hari, Wong, Liang Jie, Kalyan, Bharath, Chitre, Mandar, Vishnu, Hari, 2017. OCEANS 2017 - Aberdeen: 19–22 June 2017.
Wong, L.J., Kalyan, B., Chitre, M., Vishnu, H., 2021. Acoustic assessment of polymetallic nodule abundance using sidescan sonar and altimeter. IEEE J. Ocean. Eng. 46 (1), 132–142. https://doi.org/10.1109/JOE.2020.2967108.
Yang, K., Dong, Y., Li, Z., Wang, H., Ma, W., Qiu, Z., et al., 2024. Geochemistry of buried polymetallic nodules from the eastern Pacific Ocean: implication for the depth-controlled alteration process. Mar. Geol. 467, 107190. https://doi.org/10.1016/j.margeo.2023.107190.
Yoo, C.M., Joo, J., Lee, S.H., Ko, Y., Chi, S.-B., Kim, H.J., et al., 2018. Resource assessment of polymetallic nodules using acoustic backscatter intensity data from the Korean Exploration Area, Northeastern Equatorial Pacific. Ocean Sci. J. 53 (2), 381–394. https://doi.org/10.1007/s12601-018-0028-9.